On the Appearance of Translucent Edges: Supplementary Material

Ioannis Gkioulekas
Harvard SEAS
igkiou@seas.harvard.edu

Bruce Walter
Cornell University
bruce.walter@cornell.edu

Edward H. Adelson
Massachusetts Institute of Technology
adelson@csail.mit.edu

Kavita Bala
Cornell University
kb@cs.cornell.edu

Todd Zickler
Harvard SEAS
zickler@seas.harvard.edu

Abstract

In the supplementary material, we provide additional results and discussion of several parts of the main paper.

1. Effects of Non-Idealities

In this section, we show simulations for studying the effects of non-idealities of the wedge geometry on edge radiance profiles. These simulations complement the discussion fo Section 4 of the main paper.

Figures 1 and 2 show simulations for the effect of using a non-orthographic camera. We show simulations for two different phase functions, high-variance and isotropic respectively. In each case, we simulate camera angular extents up to $20°$. In all cases, the use of a non-orthographic camera has little effect on the shape of the radiance profiles.

Figures 3 and 4 show similar simulations where, instead of the camera, the illumination angular extent is varied. As before, the use of not perfectly collimated light has negligible effect on the shape of the radiance profiles.

Figure 5 shows simulations for the effect of surfaces that are not perfectly smooth on radiance profiles. we use a realistic microfacet refraction model [2], and render the edge radiance profile for increasing values of a parameter α controlling the roughness of the surface. A value $\alpha = 0$ means a perfectly smooth surface, $\alpha = 0.1$ is relatively rough, and $\alpha > 0.4$ is very rough surfaces (e.g., etched surface). The simulations shown are for different phase function and geometry configurations. We observe that the radiance profile maintains its characteristic features for a reasonable range of smoothnes.

Finally, Figure 6 shows rendered profiles for bevels of increasing radius, as fractions of the field of view. We ob-
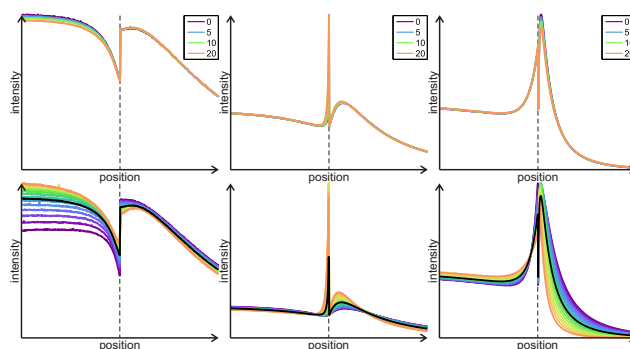

Figure 1: Simulations of sensitivity of edge radiance profiles to deviations from an orthographic camera model for a high-variance phase function. The top row compares edge radiance profiles for different anglular extents subtended by camera pixels. The bottom row shows how the edge radiance profile changes within an angle of $20°$ around the corresponding central view direction (shown in black). The average of the profiles in the bottom row produces the profile for shown in the top row for an angle of $20°$. Different columns correspond to different central view directions (left: $\theta_v = 25°$, middle: $\theta_v = 45°$, right: $\theta_v = 65°$).

serve that, for small values of the radius, the bevel effectively "erases" all interesting features that are within distance roughly equal to the radius from the geometric edge, while leaving the rest of the profile relatively uneffected.

1.1. Profile Fitting

In this section, we describe the algorithm we use in the preprocessing stage of Section 5 of the main paper, to produce analytic fits to rendered edge radiance profiles.

We use the database of profiles described in Section 2 of the main paper, and search for a parametric expression that fits all of the profiles in this database, using the insights from
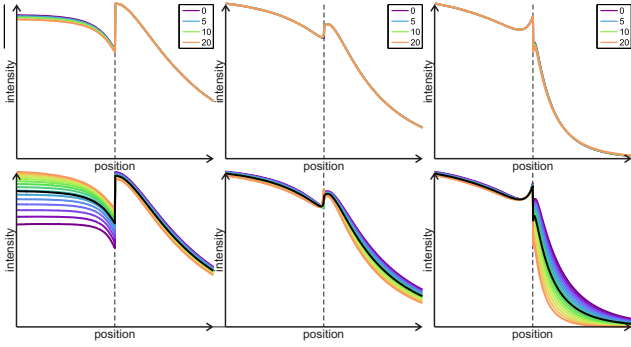
Figure 2: Simulations of sensitivity of edge radiance profiles to deviations from an orthographic camera model for an isotropic phase function. The top row compares edge radiance profiles for different anglular extents subtended by camera pixels. The bottom row shows how the edge radiance profile changes within an angle of $20°$ around the corresponding central view direction (shown in black). The average of the profiles in the bottom row produces the profile for shown in the top row for an angle of $20°$. Different columns correspond to different central view directions (left: $\theta_v = 25°$, middle: $\theta_v = 45°$, right: $\theta_v = 65°$).
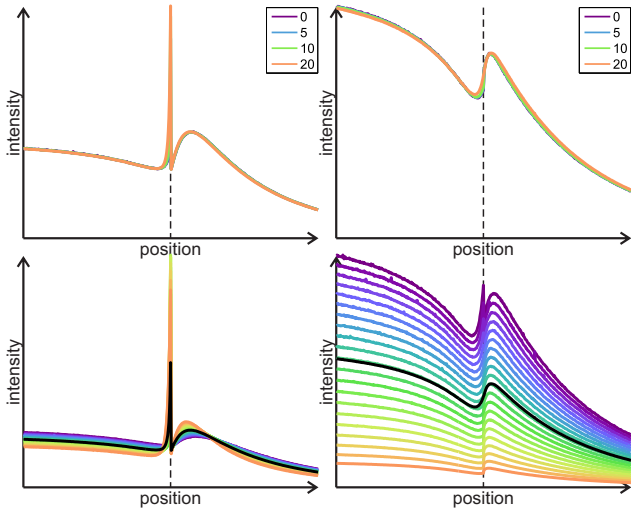

Figure 3: Simulations of sensitivity of edge radiance profiles to deviations from collimated illumination for a high-variance phase function. The top row compares edge radiance profiles for different illumination angular extents. The bottom row shows how the edge radiance profile changes within an angle of $20°$ around the corresponding central illumination direction (shown in black). The average of the profiles in the bottom row produces the profile shown in the top row for an angle of $20°$. Different columns correspond to different central illumination cdirections (left: $\theta_l = 45°$, right: $\theta_l = 75°$).
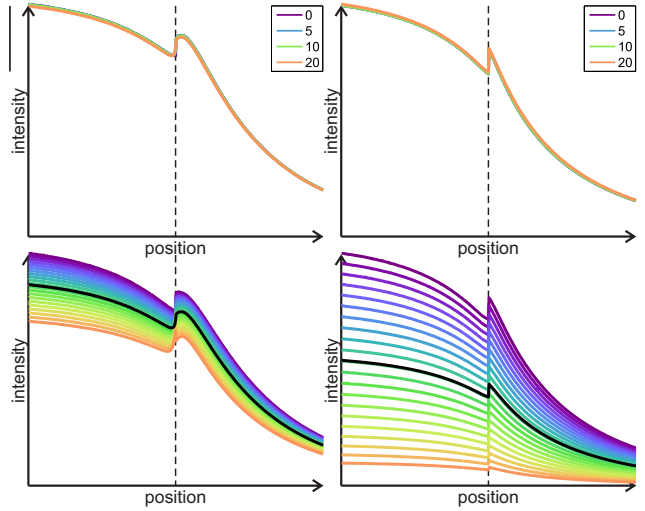

Figure 4: Simulations of sensitivity of edge radiance profiles to deviations from collimated illumination for an isotropic phase function. The top row compares edge radiance profiles for different illumination angular extents. The bottom row shows how the edge radiance profile changes within an angle of $20°$ around the corresponding central illumination direction (shown in black). The average of the profiles in the bottom row produces the profile shown in the top row for an angle of $20°$. Different columns correspond to different central illumination cdirections (left: $\theta_l = 45°$, right: $\theta_l = 75°$).
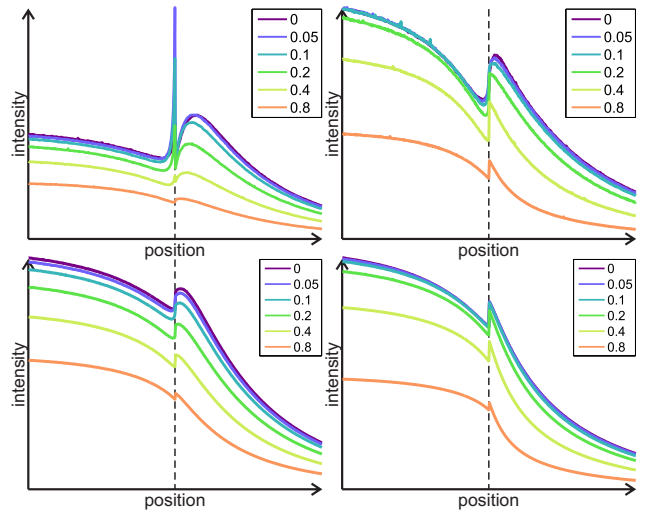

Figure 5: Simulations of sensitivity of edge radiance profiles to surface roughness. The top row shows simulations for a high-variance phase function, and the bottom row for an isotropic phase function. The two columns correspond to different illumination directions (left: $\theta_l = 45°$, right: $\theta_l = 75°$).
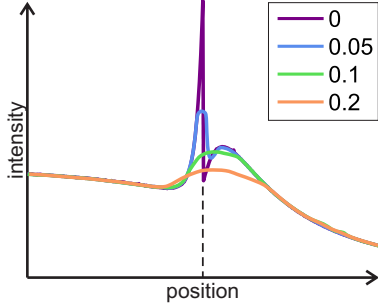
Figure 6: Simulations of sensitivity of edge radiance profiles to edge bevels, for a high-variance phase function. The values in the legend show the diameter of the bevel as a fraction of the field of view (length of "position" axis).

Section 3 of the main paper. We separately consider the four distinct regions we identified in Figure 3 of the main paper.

Regions 1 and 3 are relatively smooth, and we find they can be well approximated with general (five-parameter) fourth-degree polynomials. In regions 2 and 4 we expect that an exponential function is required at least, since we know from the single scattering component (Figure 4 of the main paper) that they are directly affected by the exponential attenuation inside the volume. Empirically, we find that these they require super-exponential functions, and we obtain good fits using a compositions of an exponential with a general fourth-degree polynomial ($\exp x^4$ rate, five parameters).

To produce a fit, we need to determine the point x where the transition from the polynomial form of region 1 to the exponentiated polynomial form of region 2 happens, and similarly the transition point from from region 3 to region 4. Empirically, we find that the transition points that result in minimum reconstruction errors do not necessarily coincide with the local extrema $x_{\min}$ and $x_{\max}$ (Figure 3 of the main paper). Instead, we determine the transition points by using grid search: we evaluate the reconstruction error for all possible locations (up to pixel grid) of the transition point from region 1 to region 2 left of the geometric edge, and select the position that minimizes the error. Similarly for the transition point from region 3 to region 4.

Following the determination of the transition points, we perform least-squares polynomial fits to regions 1 and 3, and least-squares polynomial fits to the logarithms of radiance in regions 2 and 4. This gives 5 parameters for each region, for a total of 20 parameters after determination of transition points. We experimented additionally with enforcing smoothness (continuity of first derivate) between regions 1 and 2 and regions 3 and 4, which reduces the degrees of freedom to 18. However, in most cases we found that this did not affect the results of the subsequent feature extraction stage, and therefore did not use the smoothness constraints.

The above design is based on quantitative experiments we performed using the database of edge radiance profiles described in Section 2 of the main paper, available on the project website [1]. For each of these profiles, we computed least-squares fits using the above procedure, using either second or fourth-degree polynomials for each of regions 1 to 4. Figure 7 shows the fits produced using second and fourth- degree polynomials for a random selection of profiles from the dataset. We observe that, in all cases, both algorithms give close fits to the ground-truth profile. However, in cases where the profile has prominent local extrema (local minimum left of the edge and local maximum right of the edge), the fits using second-degree polynomials cannot reproduce well the positions and values of the extrema, as the $\exp\left(x^2\right)$ rates are slower than the very fast rates of change in the profile following the extrema. In our experiments, we found that fits using fourth-degree polynomials achieve, on average across our dataset, approximately one third the root-mean-square error of fits using second-degree polynomials.

2. Effects of Scattering Material Parameters

In this section, we expand the discussion of Section 5.1 of the main paper, about the effects of scattering material parameters on edge radiance profiles.

Figure 8 shows larger versions of the graphs in the insets of Figure 8 of the main paper. The legends in the second and third columns identify corresponding phase functions. "g0.8_g-0.8_w0.7" means a phase function that is the linear combination of a forward $g = 0.8$ Henyey-Greenstein and a backward $g = -0.8$ Henyey-Greenstein lobe, with the mixture weight of the forward lobe being $w = 0.7$ and the weight of the backward lobe $1 - w = 0.3$. Similarly for other phase functions.

As discussed in Section 5.1 of the main paper, increasing the second moment of the phase function results in the positions of the local extrema in the edge profiles moving farther from the geometric edge. To understand this effect better, we use Figure 9. The left column of this figure corresponds to the same material and geometry configuration as the left column of Figure 6 of the main paper, which uses a high-variance phase function (linear combination of a forward $g = 0.8$ and backward $g = -0.8$ Henyey-Greenstein lobe with equal weight $w = 0.5$ for the two lobes; also shown in orange in the inset at the top of Figure 9). The right column of Figure 9 shows the edge radiance profile with all geometry and material parameters the same, except for the phase function which is now isotropic (Heneyey-Greenstein
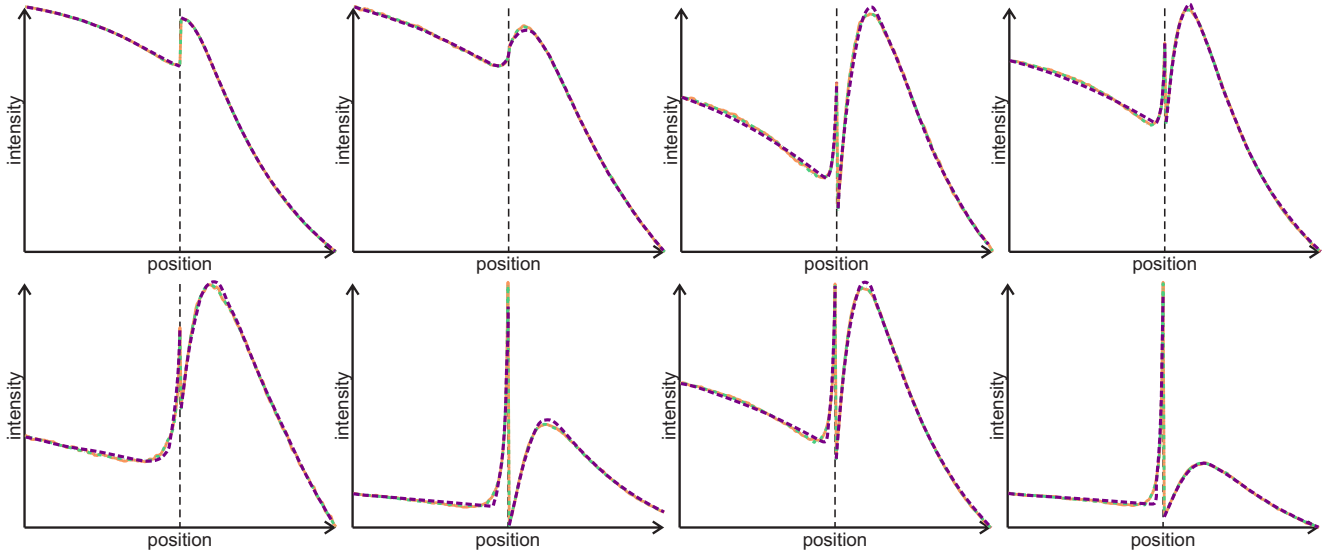
Figure 7: Analytic fits to a random selection of edge radiance profiles. In orange are the ground-truth, rendered profiles. In green are shown the fits produced using fourth-degree polynomials, and in purple the fits produced using second-degree polynomials.
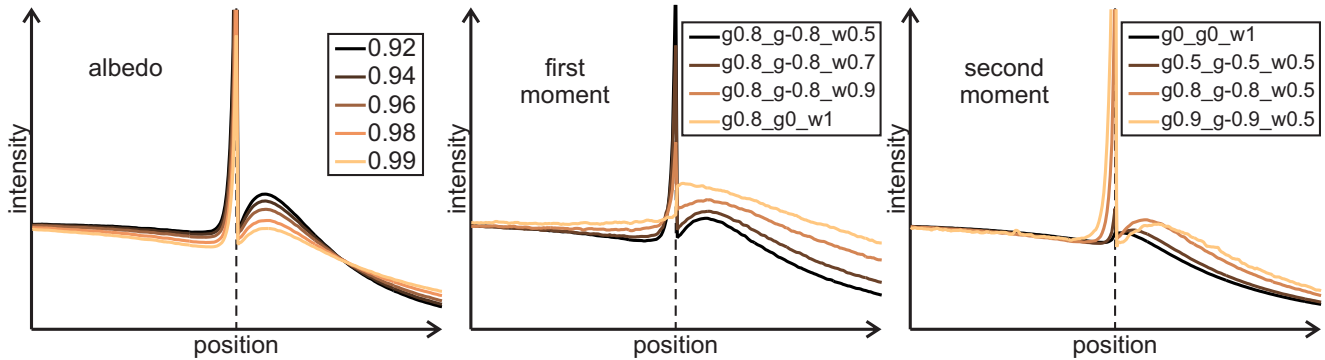

Figure 8: Effect of scattering material parameters on edge radiance profiles. Each graph shows representative sets of profiles as only the indicated parameter changes, with all other material and geometry parameters fixed. From left to right: albedo, first moment of the phase function, second moment of the phase function. Compare with Figure 8 of the main paper.

lobe with $g = 0.8$, shown in the inset in purple). These two phase functions have the same first moment, but the isotropic has a significantly smaller second moment.

As seen in Figure 9, in the case of the isotropic phase function, the positions of the two local extrema have moved so close to the edge that they are no longer visible at this resolution. In other words, with respect to the characterization of distinct regions we adopted in Figure 3 of the main paper, the edge radiance profile for the isotropic phase function only exhibits regions 1 and 4. The reason for this behavior is related to the blurring of the internal reflection boundary in mid-order scattering, as discussed in Section 3.3 and Figure 6 of the main paper. Because the isotropic phase function scatters strongly in all directions, it blurs the boundary

between the high-flux and low-flux regions of the wedge volume much faster than the high-variance phase function. To demonstrate this, we show in the second row of Figure 9 decompositions of the two edge radiance profiles into single, first, second, and so on scattering components. In both cases, the single-scattering profile is constant left of the edge, as explained in Section 3.3 of the main paper. The exponential rise left of the edge, created due to the blurring of the reflection boundary by subsequent scattering events, disappears almost immediately in the case of the isotropic phase function (only visible in the second scattering component). On the other hand, in the case of the high-variance phase function, the rise is visible in scattering components as high as the seventh. As a result, the exponential rise is
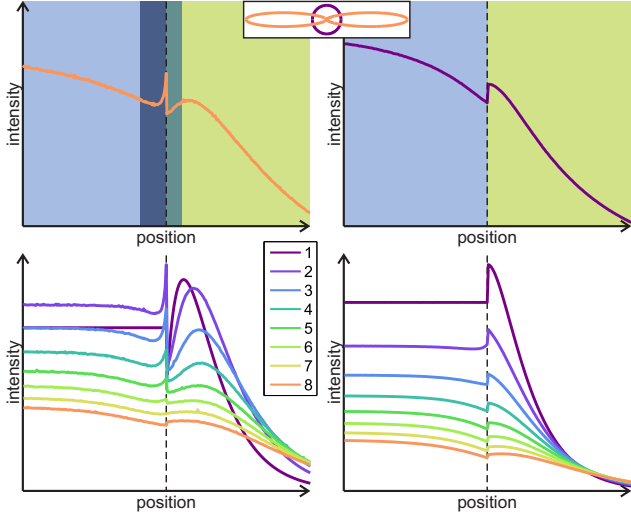
Figure 9: Effect of second moment of the phase function on edge radiance profiles. Top row: comparison of edge radiance profiles for two phase functions, shown in radial plots in the inset. Bottom row: decomposition of edge radiance profiles into separate scattering components.

visible in the full profile in the left column, but not in the right.

3. Effect of Refraction and Geometry Parameters

In this section, we expand the discussion of Section 5.2 of the main paper, about the effects of refraction and geometry parameters on edge radiance profiles.

Figure 10 shows larger versions of the graphs in the insets of Figure 9 of the main paper.

In Figure 11, we discuss the effect of refraction and geometry parameters when one of the two assumptions discussed in Section 5.2 of the paper is violated. In the left column, we compare two radiance profiles for a case where the only parameter that changes is the index of refraction. For $\eta = 1.3$, the first of the two assumptions in the main paper is violated: The angle of incident of (unscattered) light rays to the right wedge surface is smaller than the critical angle. As a result, only part of the light gets internally reflected, and the other part is refracted and continues outside of the wedge volume. For $\eta = 1.4$, the angle of incidence is larger than the critical angle, and we have total internal reflection. As a result, a lot more light gets reflected and deposited in the high-flux lightfield area than before (see Figure 4 of the main paper). As discussed in Section 3 of the main paper, intersections of view rays with this high-flux area that is created due to internal reflection are the cause of the local

extrema in the radiance profiles. Therefore, in the case of $\eta = 1.4$, the local extrema are a lot more prominent than for $\eta = 1.3$. This contradicts the effects shown in Figure 9 of the main paper and Figure 10 above. The contradiction is because of the transition from partial to total internal reflection. Once the index of refraction is large enough to have total internal reflection, then the behavior changes and increases in η result in making the local extrema less prominent, as discussed in Section 5.2 of the main paper and shown in Figure 9 of the main paper and Figure 10 above.

We observe the same behavior in the right column of Figure 11, which shows profiles where only the illumination angle changes. When the illumination angle is $45°$, there is total internal reflection. When the illumination angle increases to $60°$, light is now only partially internally reflected, violating the first of the two assumptions of the main paper. As a result, the increase in illumination angle suppresses the local extrema in the radiance profile, contrary to what is described in Figure 9 of the main paper and Figure 10 above. The contradiction is because of the transition from total internal reflection to partial reflection.

Finally, the middle column shows profiles where only the view angle changes. In this case, when the view angle is $15°$, view rays left of the geometric edge diverge from the internal reflection boundary, and do not enter the high-flux lightfield. Therefore, the second of the two assumptions described in Section 5.2 of the main paper is violated. When the view angle is increased to $30°$, view rays are refracted at an angle where they now enter the high-flux area. As a result, the increase in view angle results in local extrema having higher contrast and being farther away from the geometric edge. This contradict the effects shown in Figure 9 of the main paper and Figure 10 above, and the contradiction is because of the transition described above. Once the view angle is large enough for view rays to always enter the high-flux region, then any further increases in the view angle follow the behavior described in Section 5.2 of the main paper and shown in Figure 9 of the main paper and Figure 10 above.

References

[1] Project page. http://vision.seas.harvard.edu/translucentedges/. 3

[2] B. Walter, S. R. Marschner, H. Li, and K. E. Torrance. Microfacet models for refraction through rough surfaces. *EGSR*, 2007. 1
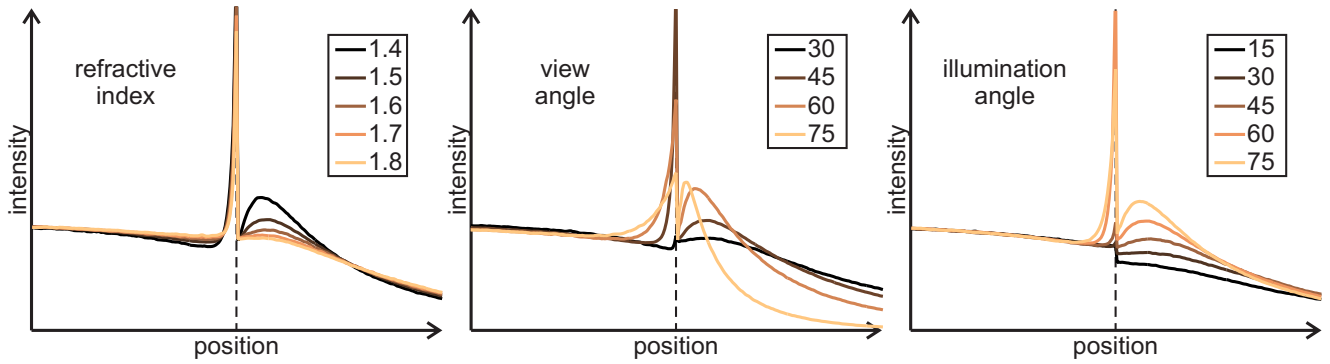
Figure 10: Effect of refraction and geometry parameters on edge radiance profiles. Each graph shows representative sets of profiles as only the indicated parameter changes, with all other material and geometry parameters fixed. From left to right: refractive index, view angle, illumination angle. Compare with Figure 9 of the main paper.
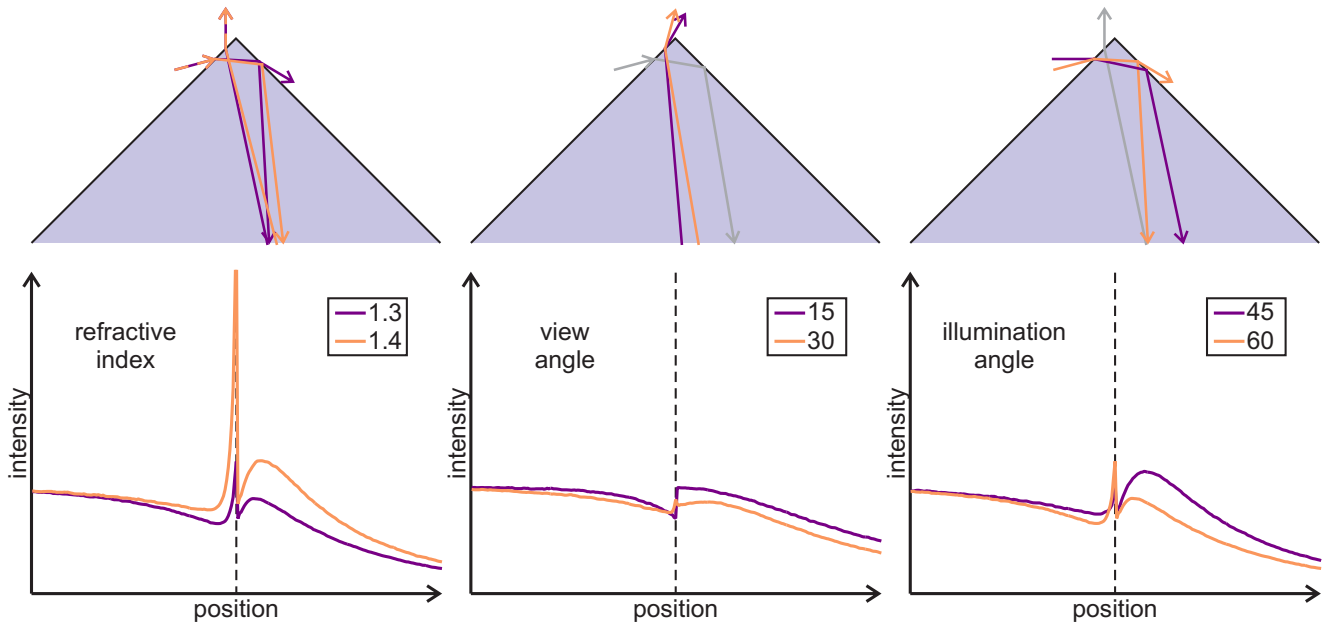

Figure 11: Effect of refraction and geometry parameters on edge radiance profiles, in cases where one of the two geometric assumptions described in Section 5.2 of the main paper are violated. For each column, the top graph shows a ray diagram and the bottom graph corresponding profiles when only the indicated parameter changes, with all other material and geometry parameters fixed. From left to right: refractive index, view angle, illumination angle. Compare with Figure 9 of the main paper.